Smart Structures and Systems, *Vol. 18, No. 3 (2016) 541-568*
DOI: http://dx.doi.org/10.12989/sss.2016.18.3.541

The effect of non-synchronous sensing on structural identification and its correction

Zhouquan Feng* and Lambros Katafygiotis[a]

Department of Civil and Environmental Engineering, The Hong Kong University of Science and Technology, Clear Water Bay, Kowloon, Hong Kong, China

(Received October 1, 2015, Revised January 8, 2016, Accepted January 30, 2016)

Abstract. The goal of this study is to investigate the effect of non-synchronous sensing when using wireless sensors on structural identification and to attempt correcting such errors in order to obtain a better identification result. The sources causing non-synchronous sensing are discussed first and the magnitudes of such synchronization errors are estimated based on time stamps of data samples collected from Imote2 sensors; next the impact of synchronization errors on power spectral densities (PSDs) and correlation functions of output responses are derived analytically; finally a new method is proposed to correct such errors. In this correction method, the corrected PSDs of output responses are estimated using non-synchronous samples based on a modified FFT. The effect of synchronization errors in the measured output responses on structural identification and the application of this correction method are demonstrated using simulation examples. The simulation results show that even small synchronization errors in the output responses can distort the identified modal and stiffness parameters remarkably while the parameters identified using the proposed correction method can achieve high accuracy.

Keywords: wireless sensor; non-synchronous sensing; structural identification

1. Introduction

Structural health monitoring (SHM) has emerged as an active, interdisciplinary research field over the past two decades due to the need to better manage and maintain complex structural systems to ensure their safety, serviceability and sustainability. Structural health monitoring employs sensing technologies and data processing methods to perform condition assessment and damage detection of structural systems, such as buildings, bridges, aircrafts and ships. A traditional SHM system usually consists of many sensors, signal transmitting wires, data acquisition (DAQ) instruments, and a centralized server for data storage and processing. However, because of the size and complexity of modern civil structures, cabling can become a troublesome issue due to high installation and maintenance costs and labor-intensive deployment. With recent advances in wireless technology, wireless sensor networks (WSNs) can solve the cabling problem. Compared to traditional wired systems, there is no extensive wiring between sensors and data acquisition system, allowing for fast and flexible deployment, easier maintenance and cost reduction. In

*Corresponding author, Ph.D., E-mail: zqfeng@outlook.com
[a] Professor, Email: lambros@ust.hk

http://www.techno-press.org/?journal=sss&subpage=8 ISSN: 1738-1584 (Print), 1738-1991 (Online)

addition, WSNs allow sensor data to be processed locally at each sensor node, which can reduce the amount of data that need to be transmitted and distribute the computing burden. These features highlight the potential of dense deployment of wireless sensors for monitoring large-scale civil infrastructures. Inspired by these advantages, WSNs are becoming immensely popular in structural monitoring and control applications (Lynch and Loh 2006, Lynch 2007, Wang *et al*. 2007).

Though densely deployed wireless sensors have the potential to improve SHM dramatically, limited hardware resources of wireless sensors with compact size preclude direct application of traditional monitoring strategies when using wireless sensor networks (Nagayama *et al*. 2007). Time synchronization in wireless sensor networks has been an important concern in the application of these networks since vibration-based structural health monitoring requires synchronous measured data from the structures. However, each wireless sensor in the network has its own intrinsic clock providing timing signals. The clocks on the sensors have to be frequently synchronized with each other to maintain a consistent global time. A number of methods have been developed and tested on clock synchronization (Sundararaman *et al*. 2005). Different algorithms and hardware resources may result in different precision. Among them, the flooding time synchronization protocol (FTSP) (Maróti *et al*. 2004) is one of the popularly adopted protocols for clock synchronization, which ensures accurate clock synchronicity among sensor nodes. For example, Imote2 nodes employing FTSP are reported to synchronize with each other with absolute error typically below 10 μs and consistently below 80 μs (Nagayama and Spencer Jr. 2007). The clock synchronization is periodically performed to eliminate the clock offset and skew. Recently, nonlinear clock drift due to extended data collection time and temperature variations have also been addressed (Li *et al*. 2015). Thus fine clock synchronization among sensor nodes has been shown to be achievable.

However, precise clock synchronization does not guarantee sensing synchronization due to inherent hardware and software limitations, which will be discussed later. One of the approaches to achieve synchronized sensing is rigorous sensing time control, which was pursued and demonstrated by Kim *et al*. (2007). Nevertheless, such approach can be computationally expensive and sometimes impractical. Another approach to achieve sensing synchronization is post-processing of the non-synchronously sensed data to eliminate such synchronization errors. This alternative approach relaxes the need for rigorous sensing time control and can tolerate some sensing synchronization errors (Nagayama and Spencer Jr. 2007, Yan and Dyke 2010).

In this article, the sources causing non-synchronous sensing are first discussed and estimated based on time stamps of data samples collected from Imote2 sensors. Then the impact of sensing synchronization errors on PSDs and correlation functions of output responses are investigated, and a new methodology for correcting such errors is proposed. Finally, the effect of non-synchronous sensing on structural identification and its correction using the proposed method is illustrated by numerical examples using simulated data.

2. Synchronization error source analysis and sampling time modeling

2.1 Sources causing non-synchronous sensing

There are many potential sources causing non-synchronous sensing in wireless sensor networks. Generally, sensing using wireless sensors is performed in the following way. Prior to sensing, clock synchronization is performed to convert local time to global time using the estimated offsets and skews between local clocks and reference clock. After clock synchronization, the gateway node sends sensing parameters such as sampling frequency and number of data points to be collected to remote nodes. When the preset start-sensing time comes, sensing tasks are posted on remote nodes. Once the sensing driver is ready, sensing starts. The sensing tasks continue running until the predetermined amount of data is acquired. During sensing, the acquired data points are first stored in a buffer. Every data point or several data points can be marked with a local time stamp (The time stamp is the time information identifying when a certain event occurred, and in the sensing application, it is the sampling time instant when a certain data point was sampled.). When the buffer is filled, the data are passed to the application designed for processing and transmitting, and then the buffer is returned to be used for the next block of data.

Potential sources causing non-synchronous sensing are summarized below (Nagayama and Spencer Jr. 2007). The schematic diagram depicting non-synchronous sensing is shown in Fig. 1.

(a). Clock synchronization error: less than 10 μs for most of the time, the upper-bound is 80 μs for Imote2 sensors with FTSP clock synchronization protocol. This error is comparatively small for SHM applications.

(b). Non-simultaneity in sensing start-up: starting the sensing tasks at all of the Imote2 nodes simultaneously is a challenge. Even if the time for starting the sensing is set to be the same global time, the real execution time is different for each node, and thus sensing will not start simultaneously.

(c). Differences in sampling frequency among sensor nodes: the sampling frequency may differ from the nominal value by at most 10 percent for the Imote2 basic sensor board.

(d). Non-uniform sampling interval over time: a non-uniform sampling interval was observed in the Imote2 sensor boards. The coefficient of variation of the sampling interval is about 0.01%~0.03%, which is relative small.

2.2 Modeling of non-synchronous sampling time

Ideally, the data are sampled uniformly (with the same constant sampling interval T_s) and synchronously (all the sensors start up sensing at the same global time). Thus, theoretically, the time at k^{th} sampling instant is

$$t_k = kT_s \tag{1}$$

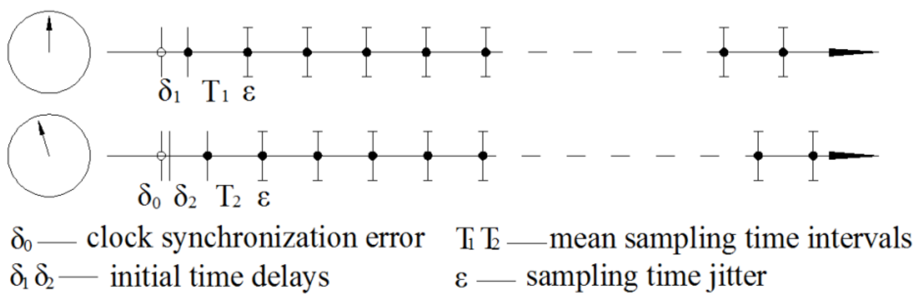

Fig. 1 Illustration of non-synchronous sensing

However, due to the reasons mentioned above, the signals are sampled at a different time instant

$$t_k' = kT_s + \delta + ck + \varepsilon(k) \tag{2}$$

where, δ is the constant time shift, coming from sources (a) and (b) mentioned in Section 2.1; because the clock synchronization error is relatively small and it is hard to be measured during sensing, only the time delay of sensing start-up is considered here as the factor contributing to the constant time shift. ck is the linear time shift, coming from source (c) mentioned in section 2.1; $c=T_s'-T_s$ is the difference between the real sampling interval T_s' and the nominal sampling interval T_s . $\varepsilon(k)$ is the random time shift with zero mean, coming from source (d) mentioned in section 2.1; these time jitters cause non-uniform sampling.

Because $\varepsilon(k)$ is relatively quite small according to test results, only the first two terms (δ and ck) are considered here. Denote the synchronous and non-synchronous data samples at the k^{th} time instant as $x(t_k)$ and $x(t_k')$ respectively, then

$$x(t_k') = x(\alpha t_k + \delta) \tag{3}$$

where $\alpha = T_s'/T_s = 1 + c/T_s$ is the scale factor of sampling interval.

3. Estimation of sensing synchronization errors

The methods for estimating sensing synchronization errors can be classified into two categories: indirect methods and direct methods. Indirect methods estimate the time delay between two measurements based on sampled data recordings. Lei *et al*. (2005) proposed two algorithms for time delay estimation: the time-delay between an output measurement and the input is estimated based on an ARX model from the input-output pair data recordings; the time-delay between two output signals is evaluated based on an ARMAV model from two output data recordings. Shen *et al*. (2012) employed cross-correlation analysis for identifying the time delays between a time-shifted wireless signal and a reference signal. However, these indirect methods only considered synchronization errors due to time delays while the synchronization errors due to sampling frequency deviation were not addressed. Moreover, these methods are only applicable in the case when the time delays are sufficiently large (at least larger than one sampling interval). On the other hand, direct methods are straightforward when the time stamps of the sampled data are available. Since wireless sensors are smart sensors with an embedded processing unit that can provide support for various modes of operation and interfacing, time stamp recording becomes achievable. Using proper embedded programming, the sensing application in wireless sensors can provide sampling time information along with the sampled data. Every data point or several data points can be marked with a local time stamp. As a result, the magnitudes of sensing synchronization errors in wireless sensors can be evaluated based on these time stamps.

In this paper, the Imote2 platform is used as the test bed. The Imote2 is an advanced wireless sensor node platform developed at Intel that became commercially available first by Crossbow Technology, Inc. (now acquired by MEMSIC, Inc.). It has a low-power processor with variable processing speed (13–416MHz) to optimize power consumption. It incorporates a Zigbee Radio with an onboard antenna. It has 256 KB of SRAM, 32 MB of external SDRAM, and 32 MB of flash memory. These unique features of the Imote2 make it suitable for SHM applications that pose high computational demands and require high-frequency sampling rates. Each sensing unit consists of an Imote2 board, a sensor board and a battery board, which are stack together via connectors (Fig. 2). One option for sensing with the Imote2 is to utilize a basic sensor board developed by Intel, available from MEMSIC Inc. This basic sensor board has a 3-axis digital accelerometer, a relative humidity sensor, a temperature sensor, a light sensor, and a general purpose 12-bit ADC. In this test, only accelerometer sensor was used.

To evaluate the magnitudes of sensing synchronization errors, a group of ten Imote2 sensors were installed and programmed with the sensing application provided by the ISHMP toolsuite (http://shm.cs.uiuc.edu), an open source software platform that contains a library of services for SHM applications and was developed by a research group at the University of Illinois at Urbana-Champaign. The accelerometer sensor boards used for testing were ITS400CB Intel Basic Sensor Boards. One of these ten sensors served as gateway node, and the other nine sensors served as remote nodes. During sensing, the time stamp of every data point was recorded. The sampling interval was calculated as the difference of two consecutive time stamps. Processing these sampling time stamps data, the magnitudes of sensing synchronization errors in Imote2 with ITS400CB sensor boards were estimated.

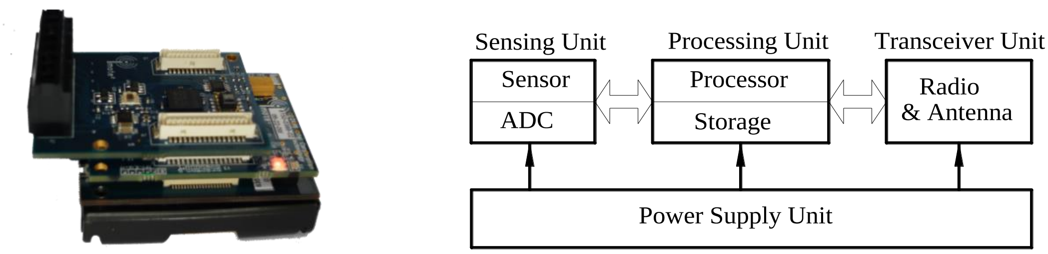

(a) Imote2 stacked configuration (b) Imote2 basic components

Fig. 2 Imote2 wireless sensor configuration and its basic components

Table 1 Statistics of sampling intervals (40 Hz, 1000 points)

Node ID	$\bar{f}_{si}$ (Hz)	$\overline{\Delta t}_i$ (μs)	Error	SD	CV
3	38.64	25878	3.51%	3.0	0.01%
32	39.09	25584	2.33%	3.8	0.01%
98	38.20	26179	4.71%	3.7	0.01%
99	39.84	25099	0.40%	2.5	0.01%
101	40.50	24690	-1.24%	2.9	0.01%
102	40.47	24711	-1.16%	4.1	0.02%
104	39.22	25499	1.99%	4.6	0.02%
105	39.98	25011	0.04%	3.0	0.01%
113	38.77	25791	3.16%	5.2	0.02%

Notes: $\bar{f}_{si}$—mean sampling frequency; $\overline{\Delta t}_i$—mean sampling interval

Table 2 Differences in the start-sensing time (Node 113 as reference)

Node ID	3	32	98	99	101	102	104	105	113
δ_i (μs)	14942	14160	16582	16582	8601	910	17908	10484	0
δ_i / Δt_i^n	0.60	0.57	0.66	0.66	0.34	0.04	0.72	0.42	0

Notes: δ_i —start-sensing time delay compared to reference node; Δt_i^n —nominal sampling interval (25ms)

From Table 1, it can be seen that the actual sampling frequencies of the accelerometers on ITS400CB sensor boards have non-negligible deviations from the nominal value. According to the data sheet of the accelerometer, which is provided by the manufacturer, the actual sampling frequency may differ from the nominal value by at most 10%. Such deviations were observed in these nine sensor boards, with a maximum observed error of 4.71% in Node 98 for sampling interval. Differences in the sampling frequencies among the sensor nodes will result in inaccurate estimation of modal parameters and stiffness parameters unless appropriate post processing is performed. The standard deviation (SD) and coefficient of variance (CV) of the sampling intervals in each sensor are listed in the last two columns of Table 1. The sampling time interval fluctuates with CV about 0.01~0.02%, which is quite small, thus can be neglected.

From Table 2, it can be seen that the sensing start-up at all of the Imote2 sensor nodes is not simultaneous. Some of them will start earlier, while some of them will start later. In this test, Node 113 is the first one to start sensing, while Node 104 is the last one to start sensing. Although the commands to start sensing are set at exactly the same time, the execution time of the commands is different on each node. This is due to the resource limitations of the embedded system, which leaves user little control to assign priority to commands. Thus, the measured signals are not synchronized to each other because of the different sensing start-up time.

4. The effect of sensing synchronization on structural identification

4.1 The effect of sensing synchronization errors on PSDs and correlation functions

The Fourier transform of a stationary random time history record $x(t)$ is defined as

$$X(f) = \int_{-\infty}^{\infty} x(t) e^{-j2\pi ft} dt \tag{4}$$

Note that physical frequency in *Hz* rather than circular frequency in *rad/s* is used in Eq. (4). All spectral quantities in this paper are with respect to the physical frequency in *Hz*. In reality, one can measure $x(t)$ only over some finite time duration T, so that $X(f)$ is estimated by computing the finite Fourier transform

$$X_T(f) = X(f, T) = \int_0^T x(t) e^{-j2\pi ft} dt \tag{5}$$

The two-sided cross spectral density function between two random processes $x(t)$ and $y(t)$ is defined by (Bendat and Piersol 1993)

$$S_{xy}(f) = \lim_{T\to\infty} \frac{1}{T} E[X^*(f,T)Y(f,T)] \tag{6}$$

where $(\cdot)^*$ denotes transpose and complex conjugate operation. Note that this definition of cross spectral density function is identical to the corresponding function defined in terms of Fourier transform of the correlation function

$$S_{xy}(f) = \int_{-\infty}^{\infty} R_{xy}(\tau) e^{-j2\pi f\tau} d\tau \tag{7}$$

The identity of these two definitions is commonly referred to as the Wiener-Khinchin relationship, and is proved in the reference (Bendat and Piersol 1986).

In time domain, the relationship of non-synchronous data and synchronous data is represented by Eq. (3). In the frequency domain, the finite Fourier transform of the corresponding non-synchronous data is expressed as (Appendix I)

$$X'_T(f) = \frac{1}{\alpha} e^{j2\pi f\frac{\delta}{\alpha}} X_T(\frac{f}{\alpha}) \tag{8}$$

Let $x(t) = [x_1(t), x_2(t)...x_k(t)...x_{N_m}(t)]^T$ be the synchronous output response time histories, where N_m is the number of output measurements. The finite Fourier transform of the synchronous output response is given by

$$\mathbf{X}(f,T) = [X_1(f,T), X_2(f,T),...X_k(f,T),...X_{N_m}(f,T)]^T \tag{9}$$

Thus the power spectral density matrix of the synchronous output is given by

$$\mathbf{S}(f) = \lim_{T\to\infty} \frac{1}{T} E[\mathbf{X}^*(f,T)\mathbf{X}(f,T)] \tag{10}$$

If synchronization errors in the form of Eq. (3) are considered, the PSD matrix of measured non-synchronous output becomes

$$\mathbf{S}'(f) = \lim_{T\to\infty} \frac{1}{T} E[\mathbf{X}'^*(f,T)\mathbf{X}'(f,T)] \tag{11}$$

with (m,n) element

$$S'_{mn}(f) = \frac{1}{\alpha_m \alpha_n} e^{j2\pi f(\frac{\delta_n}{\alpha_n} - \frac{\delta_m}{\alpha_m})} \lim_{T\to\infty} \frac{1}{T} E[X_m^*(\frac{f}{\alpha_m},T)X_n(\frac{f}{\alpha_n},T)] \tag{12}$$

where δ_m and δ_n are the constant time shifts corresponding to sensors m and n respectively; α_m and α_n are the scale factors of sampling interval with respect to sensors m and n respectively. From Eq. (12), it can be seen that the cross-spectral density function of the non-synchronous signals has changed in three aspects: firstly, the magnitude is scaled with a factor of $1/(\alpha_m\alpha_n)$; secondly, the phase is shifted by $2\pi f(\delta_n/\alpha_n - \delta_m/\alpha_m)$; thirdly, the frequencies with respect to sensor m and n are changed to f/α_m and f/α_n respectively. It is noted that $X_m(f/\alpha_m)$ and $X_n(f/\alpha_n)$ correspond to different frequencies if $\alpha_m \neq \alpha_n$. If only constant shifts δ_m and δ_n exist, Eq. (12) becomes

$$S'_{mn}(f)=e^{j2\pi f(\delta_n-\delta_m)}S_{mn}(f) \tag{13}$$

Eq. (13) implies that constant time shift errors only affect the phase information of the cross spectral density and the phase changes linearly with the frequency.

When considering the cross-correlation function, according to the sampling time model of Eq. (2), it can be expressed as

$$\begin{aligned} R'_{mn}(\tau) &= E[x_m(t+\delta_m+c_m k)x_n(t+\tau+\delta_n+c_n k)] \\ &= R_{mn}[\tau+(\delta_n-\delta_m)+(c_n-c_m)k] \end{aligned} \tag{14}$$

It can be seen that there is a time shift error $(\delta_n\text{-}\delta_m)+(c_n\text{-}c_m)k$ in the cross-correlation function. Alternatively, the correlation function can also be obtained by the inverse Fourier transform of power spectral density

$$R'_{mn}(\tau)=\int_{-\infty}^{\infty} S'_{mn}(f)e^{j2\pi f\tau}df \tag{15}$$

The errors in spectral density will also propagate in the correlation function obtained through inverse Fourier transform.

4.2 Modal parameter based structural identification using output-only data

Structural identification is a necessary and important task in the course of checking the construction quality, validating or improving analytical finite element structural models, designing structural control systems, or conducting damage assessment. When field dynamic tests are performed to identify the structural model, commonly modal parameters (natural frequencies and mode shapes) are used. For the modal parameter based structural identification approaches, there are two stages: modal parameter identification followed by physical parameter identification. The modal parameters include natural frequencies, damping ratios and mode shapes. Usually, natural frequencies and mode shapes are used for physical parameter identification, while damping ratios are rarely used. Physical parameters include parameters related to mass, damping and stiffness. Herein only the stiffness parameters are considered to be identified while mass is assumed to be known with sufficient confidence and damping is not considered.

Many algorithms have been developed and used for modal parameter identification. A special class of such algorithms based on only measured output response of the system has become very popular over the last decades (Magalhães and Cunha 2011, Bart Peeters and De Roeck 2001). In output-only modal identification, the modal testing is normally done by just measuring the response of the system under ambient or operational condition. The commonly used output-only modal identification methods can be classified into two groups: (a) frequency domain approaches and (b) time domain approaches. For frequency domain methods, most of them are based on power spectral densities, such as Peak Picking (PP) method (Felber 1993), Frequency Domain Decomposition (FDD) method (Brincker *et al.* 2001), PolyMax method (Bart Peeters, *et al.* 2004) and Bayesian Spectral Decomposition (BSD) method (Feng 2013). For time domain methods, some of them are based on correlation functions, such as the Natural Excitation Technique in conjunction with the Eigensystem Realization Algorithm (NExT-ERA) (Caicedo *et al.* 2004, James *et al.* 1993, Juang and Pappa 1985) and covariance driven Stochastic Subspace Identification (SSI-COV) method (Peeters and De Roeck 1999).

Using the identified modal parameters, the physical parameters (stiffness parameters) can be identified subsequently. Given a nominal structural model and experimentally obtained modal parameters, a more accurate model can be obtained using model updating. The model updating methods can be roughly categorized into two groups: deterministic approaches (e.g., sensitivity-based finite element model updating) and probabilistic approaches (e.g., Bayesian model updating).

In this study, three output-only modal identification algorithms and a modal-based Bayesian model updating algorithm are used. For modal identification algorithms, two traditional output-only modal identification algorithms (i.e., FDD and NExT-ERA) are used here, of which one is a frequency domain method and the other one is a time domain method. Another newly developed Bayesian modal identification algorithm (BSD) and an efficient Bayesian model updating algorithm using modal data are also employed here for application demonstration. These two new algorithms are briefly introduced below.

4.2.1 BSD method

The Bayesian Spectral Decomposition (BSD) method is a new probabilistic modal identification algorithm developed by the authors (Feng 2013). With this method, not only the optimal values of the modal parameters are obtained but also their associated uncertainties are quantified. This method is inspired by the Bayesian Spectral Density Approach (BSDA) (Katafygiotis and Yuen 2001) and the Frequency Domain Decomposition (FDD) method (Brincker *et al.* 2001). Mathematical theory shows that the eigenvalues and eigenvectors of the spectral matrix follow Normal distributions. Based on these statistical properties, the optimal values of the modal parameters and their associated uncertainties are determined using Bayesian inference. The method begins with eigendecomposition of the output spectral matrix. Based on the calculated eigenvalues, the most probable values of the modal frequency and damping ratio are determined by maximizing the posterior PDF which involves the prior PDF and the likelihood function. The corresponding covariance matrix of the posterior distribution is also calculated at the most probable values. The first eigenvector at the discrete frequency that is closest to the identified modal frequency is an estimate of the mode shape with unitary normalization. The covariance matrix of the mode shape is also calculated based on the normal property of the eigenvector.

4.2.2 Efficient Bayesian model updating using modal data

Recently, an efficient approach for model updating of linear structural models with modal data was proposed by the authors (Feng and Katafygiotis 2013). The proposed method consists of two steps: preliminary model updating using a deterministic approach followed by Bayesian probabilistic model updating. In the beginning, an initial finite element (FE) model based on the design drawings and/or initial guesses is constructed. In the preliminary updating stage, an iterative technique based on the eigenvalue equation and mode shape expansion is applied to obtain an initial estimate of the stiffness parameters. Finally, a probabilistic approach based on a Bayesian framework is used to find the most probable values of the stiffness parameters as well as to quantify their associated uncertainties.

4.3 The propagation of sensing synchronization errors in structural identification process

The propagation path of the sensing synchronization errors in modal parameter based structural identification process is depicted in Fig. 3.

The effect of sensing synchronization errors on the estimation of power spectral density and/or correlation function has been derived analytically previously. The severity of further propagation of these errors in modal identification depends on the method that is employed. Different modal identification methods may have different propagation paths and effects. Many studies showed that small time delays in the measured system response can distort the identified mode shapes seriously when the FDD method is used (Krishnamurthy *et al*. 2008, Park *et al*. 2011, Yan and Dyke 2010). In this study, the effect of sensing synchronization errors (not only time delays but also sampling frequency deviations) on modal identification is studied extensively using numerical simulations and the results produced by three different methods (FDD, NExT-ERA, BSD) are compared.

The errors in modal parameters will also propagate in the identification of stiffness parameters. The propagation of mode shape errors into the flexibility matrix has been studied analytically by Mukhopadhyay *et al*. (2012). In this study, the propagation of modal parameter errors (not only mode shapes but also frequencies) on stiffness identification is also studied using numerical simulations. Bayesian probabilistic model updating method using modal data is adopted for stiffness parameters identification (Feng and Katafygiotis 2013). Such error propagations are investigated in the simulation example 2.

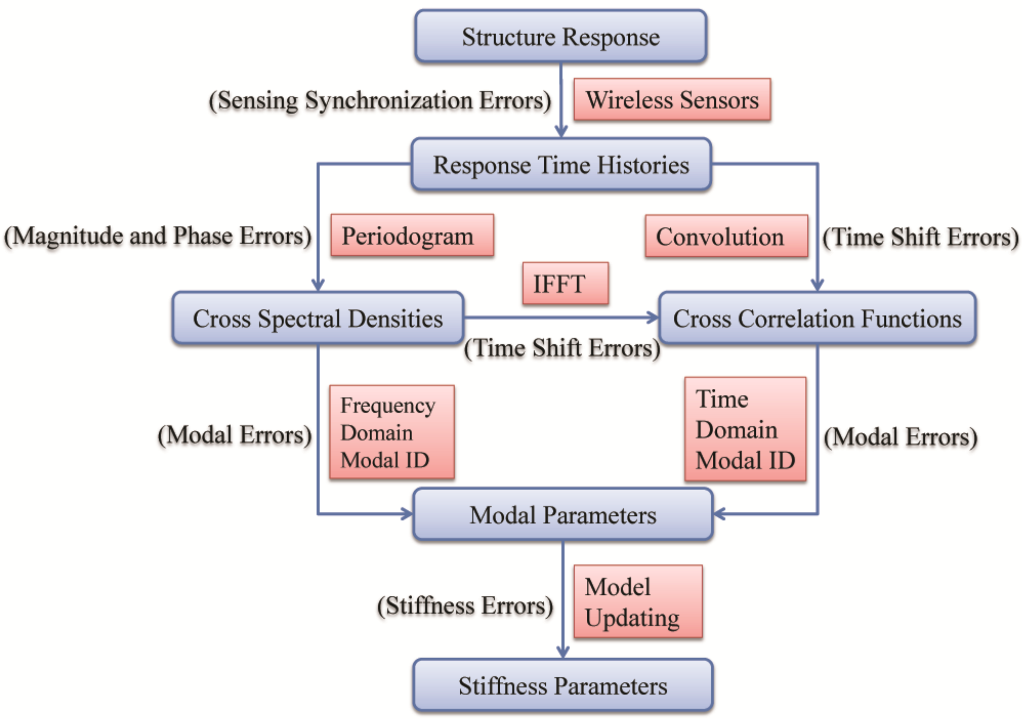

Fig. 3 The propagation path of the sensing synchronization errors in modal-based structural identification process

5. Error correction

5.1 Related work review

In order to eliminate the synchronization errors, direct intuition suggests reconstructing synchronous data from the measured non-synchronous ones. This is so called signal reconstruction, and some work has been done for this purpose, e.g., interpolation based approach (Divi and Wornell 2008) and resampling based approach (Nagayama and Spencer Jr. 2007).

The interpolation based approach is based on the Whittaker-Shannon interpolation formula. If $x(t)$ is band-limited and the sampling frequency is higher than twice the upper bound frequency, according to the Whittaker-Shannon interpolation formula, the continuous-time band-limited signal can be written as

$$x(t) = \sum_{n=-\infty}^{\infty} x(n) \cdot \mathrm{sinc}(f_s(t - nT_s)) \tag{16}$$

where $x(n)$ are discrete data samples with uniform sampling intervals, f_s is the sampling frequency $f_s=1/T_s$, and *sinc* function is defined by

$$\mathrm{sinc}(x) = \frac{\sin(\pi x)}{\pi x} \tag{17}$$

Using Eq. (16), synchronous data samples can be reconstructed by interpolation from the non-synchronous samples. However, Eq. (16) requires infinite samples theoretically, which cannot be realized. If finite samples are used, it renders big errors. It also requires a lot of computational effort.

Alternatively, synchronous data samples can be obtained by resampling from non-synchronous data samples, as it was done by Nagayama and Spencer Jr. (2007). This algorithm involves a combination of interpolation, filtering and decimation. One of the possible error sources of this resampling process is imperfect filtering. Also the FIR filter design becomes extremely challenging when the upsampling factor is large (Nagayama and Spencer Jr. 2007). The basic idea of resampling is depicted in Fig. 4.

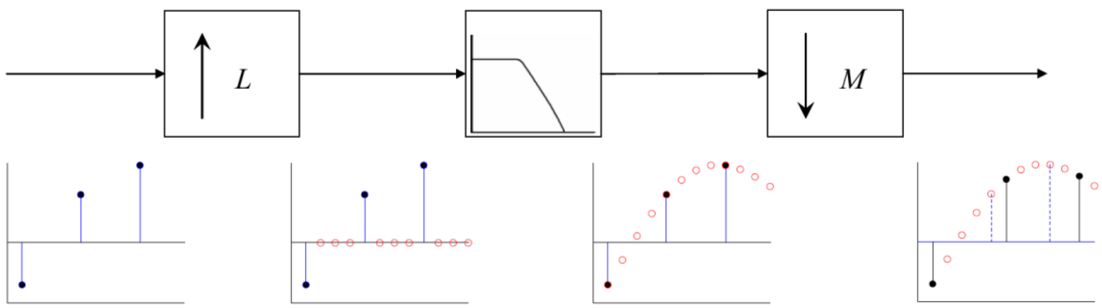

Fig. 4 Basic idea of resampling (Nagayama and Spencer Jr. 2007)

5.2 Proposed algorithm

As discussed before, signal reconstruction in time domain is computationally expensive and time-consuming. Since only spectral density or correlation function estimates are needed for most of the modal identification algorithms and raw sampled data are not needed, reconstruction of the signal in the time domain can be avoided. Rather than reconstructing the signal in the time domain, we develop a correction approach in the frequency domain to obtain an accurate spectral density using non-synchronous samples. This approach is based on the spectral relationship of synchronous data and non-synchronous data. Once the corrected spectral densities are obtained, the correlation functions can also be easily obtained by inverse Fourier transform.

5.2.1 Constant time shift

Consider two time histories $\mathbf{x}_\alpha = \{x_\alpha(0), x_\alpha(\Delta t), ... x_\alpha((N-1)\Delta t)\}^T$ and $\mathbf{x}'_\beta = \{x'_\beta(\delta), x'_\beta(\Delta t+\delta), ... x'_\beta((N-1)\Delta t+\delta)\}^T$, where $\mathbf{x}'_\beta$ has a constant time shift δ. The discrete Fourier transform (DFT) for $\mathbf{x}_\alpha$ is given by

$$X_\alpha(f_k) = \sum_{n=0}^{n=N-1} x_\alpha(n\Delta t) e^{-j2\pi f_k n\Delta t} = \sum_{n=0}^{n=N-1} x_\alpha(n\Delta t) e^{-j\frac{2\pi}{N}kn} \tag{18}$$

where $f_k = k\Delta f$, $\Delta f = 1/(N\Delta t) = f_s / N$ is the frequency resolution in *Hz* and f_s is the sampling frequency. The discrete Fourier transform for the shifted time history $\mathbf{x}'_\beta$ is given by (Appendix II)

$$X'_\beta(f_k) = e^{j2\pi f_k \delta} \cdot X_\beta(f_k) \tag{19}$$

Therefore

$$X_\beta(f_k) = X'_\beta(f_k) \cdot e^{-j2\pi f_k \delta} = X'_\beta(f_k) \cdot \left(e^{-j\frac{2\pi}{N}\frac{\delta}{\Delta t}} \right)^k \tag{20}$$

Note that Eq. (6) provides the spectral density estimate assuming continuous time and frequency. For discrete time and frequency, the cross spectral density estimate can be obtained by (Appendix III)

$$S_{x_\alpha x_\beta}(f_k) = \lim_{N\to\infty} \frac{\Delta t}{N} E\left[X^*_\alpha(f_k) X_\beta(f_k) \right] \tag{21}$$

The scaling factor $\Delta t/N$ of the spectral density estimate in Eq. (21) is defined such that the spectral density is two-sided with respect to the physical frequency in *Hz*.

5.2.2 Linear time shift

Consider two time histories $\mathbf{x}_\alpha = \{x_\alpha(0), x_\alpha(\Delta t_\alpha), ... x_\alpha((N_\alpha - 1)\Delta t_\alpha)\}^T$ and $\mathbf{x}_\beta = \{x_\beta(0), x_\beta(\Delta t_\beta), ... x_\beta((N_\beta - 1)\Delta t_\beta)\}^T$, that have different sampling frequencies, i.e., $\Delta t_\alpha \neq \Delta t_\beta$, and total sampling time lengths $T_\alpha = N_\alpha \Delta t_\alpha$ and $T_\beta = N_\beta \Delta t_\beta$, respectively. In discrete Fourier transform, we know that $f_k = k\Delta f$ and $\Delta f = 1/(N\Delta t) = f_s / N$. In order to make sure $X_\alpha(f_k)$ and $X_\beta(f_k)$ correspond to the same discrete frequency when calculating the cross spectral density, their frequency resolutions should be identical, i.e., $\Delta f_\alpha \equiv \Delta f_\beta$, thus their time duration should be the same, i.e.

$$N_\alpha \Delta t_\alpha = N_\beta \Delta t_\beta, \quad \frac{N_\alpha}{N_\beta} = \frac{\Delta t_\beta}{\Delta t_\alpha} \tag{22}$$

Based on this relationship, the cross spectral density can be estimated by (Appendix IV)

$$S_{x_\alpha x_\beta}(f_k) = \frac{\Delta t_\beta}{N_\alpha} E[X_\alpha^*(f_k) X_\beta(f_k)] = \frac{\Delta t_\alpha}{N_\beta} E[X_\alpha^*(f_k) X_\beta(f_k)], \text{ when } N_\alpha, N_\beta \to \infty \tag{23}$$

where $f_k = k\Delta f$, $\Delta f = 1/(N_\alpha \Delta t_\alpha) = 1/(N_\beta \Delta t_\beta)$, $k = 0,1,\ldots,\min\{\mathrm{int}(N_\alpha/2)+1, \mathrm{int}(N_\beta/2)+1\}$.

5.2.3 Summary of procedures

In reality, the time shifts of non-synchronous data are a combination of constant time shifts and linear time shifts as shown in Section 3. The most popular FFT-based method for power spectral density estimation is Welch's refined periodogram approach (Welch 1967). In order to obtain an accurate power spectral density estimate from non-synchronous data, the proposed procedures are as follows:

(1). Perform sensing, and make sure the time stamps are also recorded when sampling.

(2). Set one sensor as reference, and partition the data points into several segments. Each segment has a length of N_r data points (subscript r refers to reference node).

(3). Partition the data points of other sensors into several segments as well. The first data point of each segment is chosen as close as possible to that of the corresponding segment in the reference sensor data by comparing their time stamps. For sensor i, the length N_i of each segment is chosen such that Eq. (22) holds approximately.

(4). Calculate the Fourier transform of each segment and correct it using Eq. (20).

(5). Calculate the cross spectral density using Eq. (23) for each segment.

(6). Calculate the average of cross spectral densities obtained from different segments.

(7) When the cross-correlation functions are needed for modal identification, they can be calculated by inverse Fourier transform of the cross spectral densities. This step is optional, depending on the modal identification algorithm employed.

After accurate estimates of the power spectral densities or correlation functions are obtained, they are fed into a chosen modal-based structural identification algorithm for modal parameter identification followed by model (e.g., stiffness parameters) identification. The procedures of the proposed method in the application of modal-based structural identification are depicted in Fig. 5.

6. Illustration examples

6.1 Example 1: 2-DOF shear building model

As discussed earlier, power spectral densities are the basis of most modal identification algorithms and subsequent modal-based stiffness identification methods. To study the propagation of synchronization errors in power spectral densities (especially cross spectral densities), we simulated a 2-DOF structural system subjected to white noise excitation. Four cases are considered: no time shift, constant time shift, linear time shift and combination of both types of time shifts. The 2-storey shear building model is shown in Fig 6. In this system $m_1 = m_2 = 2\times10^4 kg$, $k_1 = k_2 = 6\times10^6 N/m$, the damping is assumed as Rayleigh damping such that the damping ratios are $\zeta_1 = \zeta_2 = 0.01$. The measurement noise is assumed to be 3% of the root mean square of the responses.

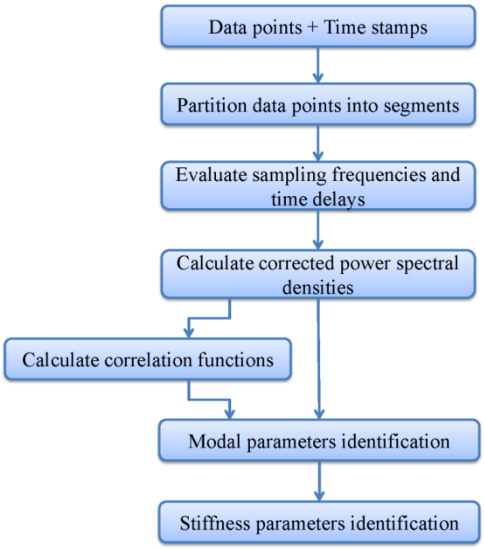

Fig. 5 Procedures of the proposed synchronization errors correction method for modal-based structural identification

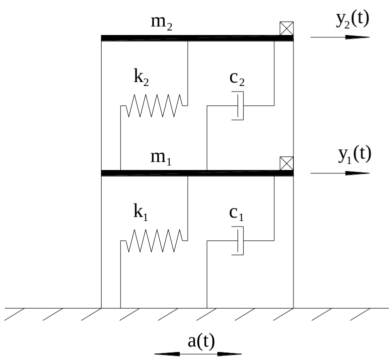

Fig. 6 Two-storey shear building model

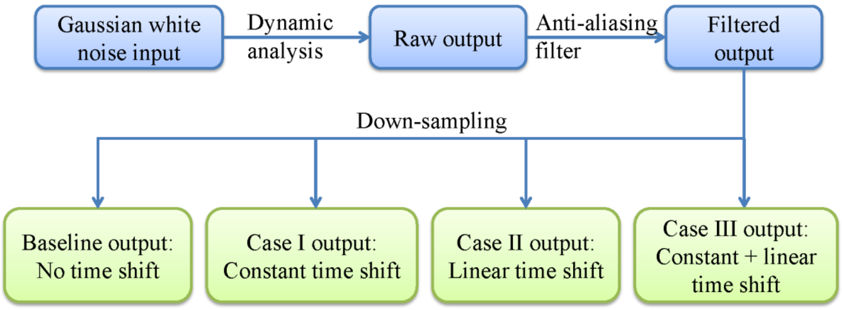

Fig. 7 Flowchart of non-synchronous sensing simulation

According to the levels of synchronization errors shown in Section 3, the simulations are performed as follows (Fig. 7):

Input: Gaussian white noise base acceleration $a(t)$, with sample frequency 10000 Hz, corresponding to sampling time interval 0.1 ms.

Raw output: Using the Matlab built-in function *lsim* (Simulate LTI model responses to arbitrary inputs), the raw output responses, also sampled at 10000Hz, are obtained.

Baseline (no time shift): Apply an anti-aliasing filter to the raw data first and then pick one data point every 250 data points from the filtered output samples for both of the two channels. The resulting new sampling frequencies for both channels are 40Hz, and the sampling time intervals are 25 ms.

Case I (constant time shift): Apply first an anti-aliasing filter to the raw data and then pick one data point every 250 data points from filtered output samples of both of these two channels, but the first data point of channel #2 has 200 points delay compared to that of channel #1. Thus, the new sampling frequencies are 40 Hz and the sampling time intervals are 25 ms for both channels, but channel #2 has a time delay of 20 ms.

Case II (linear time shift): Apply first an anti-aliasing filter to the raw data and then pick one data point every 250 data points for channel #1 and one data point every 247 data points for channel #2. The resulting sampling frequencies of channel #1 & #2 are 40 & 40.4858 Hz respectively, while the corresponding sampling time intervals are 25 ms & 24.7 ms respectively.

Case III (combinational time shift): Apply first an anti-aliasing filter to the raw data and then pick one data point every 250 data points for channel #1 and one data point every 247 data points for channel #2. The first data point of channel #2 has 200 points delay compared to that of channel #1. This case is basically the superposition of case 1 and case 2.

In the power spectral density matrix computation, the data segment lengths for FFT are chosen as 4096 points for the sampling frequency of 40 Hz, i.e., length of 102.4 sec. This number will be changed accordingly when a sampling frequency other than 40 Hz is assumed. Although overlapping and windowing are commonly employed to increase the accuracy of the spectral density estimation, no window and overlap is imposed in this study for simplification. Twenty segments of data points are used for averaging. The auto-spectral densities, the magnitude and phase spectrum of cross-spectral densities of case I, case II and case III compared with the baseline are plotted in Figs. 8-10, respectively. In these figures, the dash lines stand for the spectrum of baseline while the solid lines stand for the spectra of case I, case II and case III. The frequency values at two peaks which correspond to two modes of the structure are shown in these figures, which clearly show the frequency deviations caused by the time shift errors. The phase values at corresponding peaks are also shown in the figures, which clearly show the phase deviations caused by the time shift errors. The spectrum values at the two peaks are tabulated in Table 3. From Fig. 8 and Table 3, it can be seen that the constant time shift error almost only affects the phase information of the cross spectral density and the phase deviation depends linearly on the frequency. From Fig. 9 and Table 3, it can be seen that the linear time shift error has influence on both the auto-spectral density and the cross spectral density. For the cross spectral density, both magnitude and phase information change. When the actual sampling frequency (40.4858Hz) is larger than the nominal sampling frequency (40Hz), the corresponding frequencies at the peaks become smaller. The phase changes caused by the linear time shift errors fluctuate with frequency. For the combinational time shift of case III shown in Fig. 10 and Table 3, the frequency changes at the peaks are the same as those of the linear time shift case, while the phase changes fluctuate with frequency. These results basically confirm the analytical predictions derived in Section 4.1.

Using the proposed correction method, the corrected power spectral densities of case III are plotted in Fig. 11. It can be seen that the corrected power spectral densities agree well with the power spectral densities of the baseline case, which confirms the effectiveness of the proposed correction method. In order to compare the performance of the proposed correction method with the resampling based signal reconstruction method (Nagayama and Spencer Jr. 2007), the output responses of case III are resampled with interpolation, filtering and decimation. Firstly, the output of channel #1 is interpolated with a factor of 250 and the output of channel #2 is interpolated with a factor of 247. Then the first 200 data points of interpolated output of channel #1 are discarded to compensate the initial time delay. Finally the outputs of channel #1 and #2 pass an anti-aliasing filter and are decimated with a factor of 1/250. The power spectral densities of the resampled data are plotted in Fig. 12. The performance comparison of the proposed method with the resampling based method is tabulated in Table 4. It can be seen that the magnitude of power spectral densities for both methods agree very well with those of the baseline case. For the phase of power spectral densities, since it is more sensitive to the synchronization errors, the accuracy is not as good as the accuracy of magnitude, but it is also acceptable. Furthermore, the proposed method performs better than the resampling based method in terms of accuracy of the phase of the power spectral densities. By using Matlab 2013b on a desktop with Intel Core i7-3770 @3.4 GHz and 16 GB RAM, it takes around 1.06 seconds to implement the proposed correction method, while it takes around 130.27 seconds to implement the resampling based method.

Table 3 Spectrum values at peak frequencies in synchronous and non-synchronous sensing cases

	Baseline		Case I		Case II		Case III	
	1st Peak	2nd Peak	1st Peak	2nd Peak	1st Peak	2nd Peak	1st Peak	2nd Peak
S_{11}	0.8065	0.1380	0.8065	0.1380	0.8065	0.1380	0.8065	0.1380
$\|S_{12}\|$	1.3043	0.0850	1.3042	0.0850	0.1865	0.0108	0.1862	0.0108
S_{22}	2.1093	0.0525	2.1092	0.0524	2.1832	0.0524	2.1842	0.0523
θ_{12}	0.0016	2.9224	-0.2121	2.3612	-2.7415	1.3667	-2.9585	0.8029

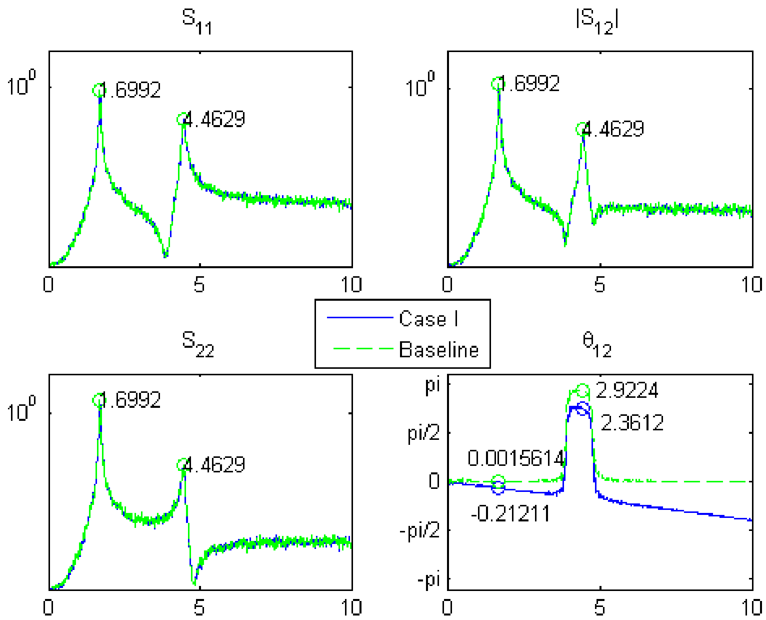

Fig. 8 Power spectral densities of constant time shift output compared with baseline

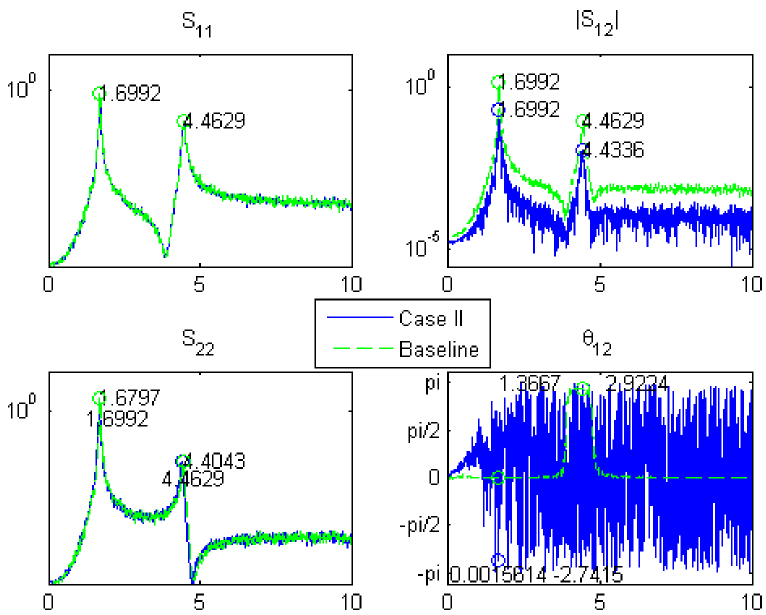

Fig. 9 Power spectral densities of linear time shift output compared with baseline

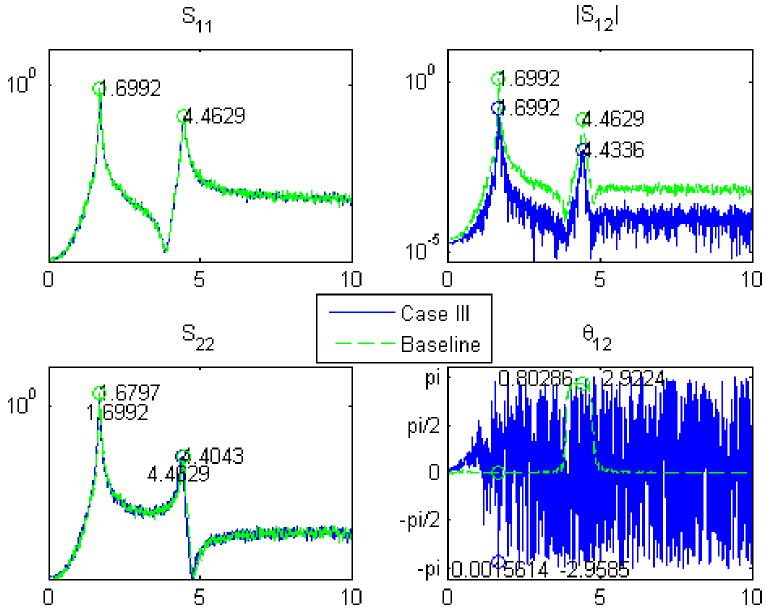

Fig. 10 Power spectral densities of combinational time shift output compared with baseline

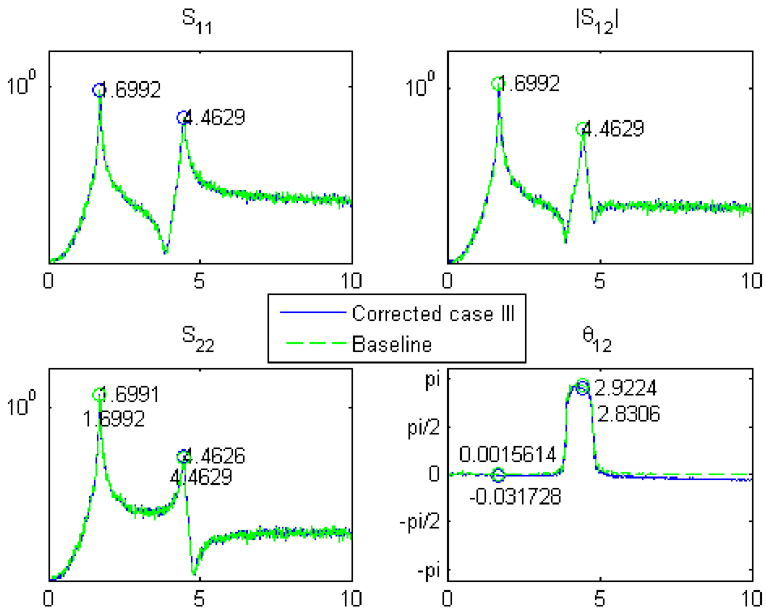

Fig. 11 Corrected power spectral densities of combinational time shift output compared with baseline

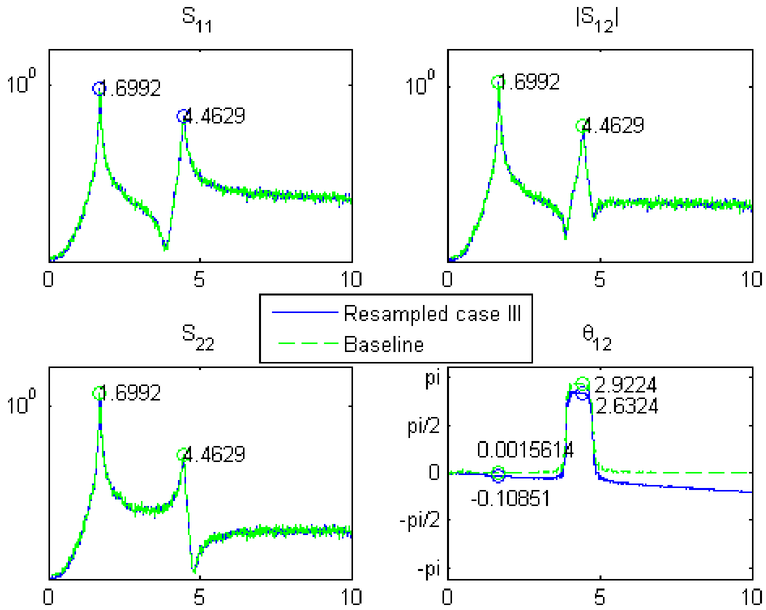

Fig. 12 Power spectral densities of resampled combinational time shift output compared with baseline

Table 4 Comparison of proposed correction method with resampling method

	Baseline		Corrected case III (1.06s)		Resampled case III (130.27s)	
	1st Peak	2nd Peak	1st Peak	2nd Peak	1st Peak	2nd Peak
S_{11}	0.8065	0.1380	0.8065	0.1380	0.7912	0.1375
$\|S_{12}\|$	1.3043	0.0850	1.3006	0.0853	1.2796	0.0847
S_{22}	2.1093	0.0525	2.0973	0.0528	2.0694	0.0522
θ_{12}	0.0016	2.9224	-0.0317	2.8306	-0.1085	2.6324

6.2 Example 2: 6-DOF shear building model

To study the propagation of synchronization errors in modal identification and subsequent modal-based stiffness identification, and to illustrate the application of the proposed algorithm for error correction in the structural identification process, simulated data using a 6-DOF shear building structure subjected to white noise excitation are considered. In this system $m_{1\sim 6} = 2\times 10^4 kg$, $k_{1\sim 6} = 4\times 10^7 N/m$, and Rayleigh damping is assumed with corresponding damping ratios $\zeta_1 = \zeta_2 = 0.01$. The theoretical modal frequencies and mode shapes are calculated and the values of the first four modes are tabulated in Table 5. All six DOFs are assumed to be measured and the measurement noise for the response is taken to be 3%. The nominal sampling frequency is assumed to be 40 Hz, while the actual sampling frequencies f_{si} (i=1,2,…6) and the relative differences of start-sensing time δ_i (i=1,2,…6) for the six channels are shown in Table 6. The magnitudes of the assumed synchronization errors are comparable to those of the estimates in Section 3.

The modal parameters are identified using three methods: FDD method, NExT-ERA method and BSD method. The modal frequencies and mode shapes identified using FDD, NExT-ERA, BSD are summarized in Table 7, Table 8 and Table 9, respectively. In each table, the identified results from synchronous data, non-synchronous data and corrected non-synchronous data are compared. In these tables, the values in the bracket are the relative errors of the identified modal frequency compared to its theoretical value; MAC denotes the modal assurance criterion between the identified mode shape and the theoretical mode shape; SD denotes standard deviation. It is seen that all of these three algorithms suffer from errors when using the non-synchronous data directly. The synchronization errors affect the identified modal frequencies only slightly while they affect the mode shapes much more. It is observed that the identified modal frequencies are larger than the theoretical values as most of the actual sampling frequencies are smaller than the nominal ones. The identified mode shapes appear to have large deviations from the theoretical ones for all methods in the case of non-synchronous data, which can be seen from the values of MAC between the identified mode shapes and the theoretical mode shapes. The effects of the sensing synchronization errors on the estimates of modal parameters are different when using different modal identification methods. Using the proposed correction method, these errors are largely eliminated and the identified modal parameters become satisfactorily accurate. From the tables, it is seen that the modal frequencies and mode shapes identified from the non-synchronous data after using the proposed correction method render similar high accuracy as those identified from the synchronous data.

Table 5 Theoretical values of modal frequency and mode shape of first four modes

Mode	Modal	Mode shapes					
number	frequency	1	2	3	4	5	6
1	1.7159	-0.1327	-0.2578	-0.3678	-0.4565	-0.5187	-0.5507
2	5.0479	-0.3678	-0.5507	-0.4565	-0.1327	0.2578	0.5187
3	8.0865	-0.5187	-0.3678	0.2578	0.5507	0.1327	-0.4565
4	10.6552	-0.5507	0.1327	0.5187	-0.2578	-0.4565	0.3678

Table 6 Sampling frequencies and relative differences of start-sensing time

	1st DOF	2nd DOF	3rd DOF	4th DOF	5th DOF	6th DOF
f_{si} (Hz)	39.2157	39.604	40.404	38.835	38.0952	38.4615
δ_i (μs)	0	11250	6500	9000	10500	7250

Table 7 Modal frequencies and mode shapes identified by FDD

	Mode number	Modal frequency	Mode shape						
			1	2	3	4	5	6	MAC
Syn.	1	1.709 (-0.4021%)	-0.1329	-0.2574	-0.3681	-0.4566	-0.5188	-0.5504	1.0000
	2	5.0586 (0.212%)	-0.3654	-0.5468	-0.4537	-0.1314	0.2605	0.5258	0.9999
	3	8.0859 (-0.0074%)	-0.5114	-0.372	0.2495	0.5544	0.1432	-0.4583	0.9997
	4	10.625 (-0.2834%)	-0.5403	0.1228	0.5264	-0.2583	-0.4649	0.3647	0.9997
Non-syn.	1	1.7773 (3.5783%)	-0.0283	-0.0235	-0.0362	0.4379	0.1069	-0.8911	0.0668
	2	5.127 (1.567%)	-0.112	0.9787	-0.1414	-0.0301	-0.0289	-0.0885	0.2329
	3	8.3105 (2.77%)	-0.4083	0.137	0.0141	-0.8953	-0.0187	0.1114	0.1454
	4	10.8789 (2.0994%)	-0.9641	0.0429	-0.1598	-0.028	-0.0112	-0.2053	0.1525
Corr. non-syn.	1	1.709 (-0.4021%)	-0.1325	-0.2577	-0.3685	-0.4554	-0.5186	-0.5512	1.0000
	2	5.0586 (0.212%)	-0.3494	-0.5529	-0.4566	-0.1258	0.2551	0.5318	0.9994
	3	8.0859 (-0.0074%)	-0.507	-0.3747	0.2518	0.5516	0.1441	-0.4626	0.9996
	4	10.625 (-0.2834%)	-0.5551	0.1157	0.5129	-0.2661	-0.4727	0.348	0.9989

In the second step, the identified modal parameters are used to update the stiffness parameters using a Bayesian probabilistic method. The stiffness matrix is parameterized using a linear model described as

$$K(\theta) = K_0 + \sum_{n=1}^{N_\theta} \theta_n K_n \tag{24}$$

where K_0 is the nominal global stiffness matrix, K_n is the corresponding n^{th} substructure stiffness matrix, and θ_n is a factor that allows for the scaling of the nominal substructure stiffness K_n so that the overall stiffness is more consistent with the actual structural behavior. In the simulations, the nominal inter-storey shear stiffnesses are assumed to be $k_{1\sim6}^0 = 5\times10^7 N/m$, which overestimate the actual stiffness parameters ($k_{1\sim6} = 4\times10^7 N/m$).

Table 8 Modal frequencies and mode shapes identified by NExT-ERA

	Mode number	Modal frequency	Mode shape						
			1	2	3	4	5	6	MAC
Syn.	1	1.7158 (-0.0058%)	0.14	0.246	0.3787	0.4514	0.5203	0.5495	0.9997
	2	5.0523 (0.0872%)	0.369	0.5496	0.4579	0.1323	-0.2574	-0.518	1.0000
	3	8.0885 (0.0247%)	0.5165	0.3663	-0.2579	-0.5518	-0.1339	0.4584	1.0000
	4	10.6676 (0.1164%)	0.5506	-0.1318	-0.5179	0.2564	0.458	-0.3684	1.0000
Non-syn.	1	1.7554 (2.3020%)	0.7872	0.2296	0.0582	-0.4979	-0.1274	-0.2453	0.0592
	2	5.1548 (2.1177%)	-0.9969	-0.0587	-0.0262	-0.0154	-0.0065	-0.0432	0.1512
	3	8.2517 (2.0429%)	0.9992	0.0176	0.0085	0.0168	0.005	-0.0297	0.2491
	4	10.8767 (2.0788%)	-0.9986	-0.021	-0.0131	0.024	0.0261	-0.029	0.2617
Corr. non-syn.	1	1.7159 (0%)	0.1422	0.2637	0.3646	0.4506	0.5255	0.546	0.9998
	2	5.052 (0.0812%)	0.3746	0.5488	0.4557	0.1339	-0.2598	-0.5152	0.9999
	3	8.0883 (0.0223%)	0.5263	0.3562	-0.2529	-0.5624	-0.1356	0.4444	0.9995
	4	10.6655 (0.0967%)	0.5687	-0.1248	-0.5012	0.2645	0.4673	-0.3485	0.9988

Using twenty realizations, twenty modal data sets are obtained using the BSD method. Each modal data set contains the optimal values of modal frequencies and mode shapes and also their associated covariance matrix. The identified modal data sets are fed into a Bayesian structural mode updating for stiffness identification (Feng and Katafygiotis 2013). The updated stiffness parameters are tabulated in Table 10. It is seen that the updated stiffness parameters using modal parameters directly identified from non-synchronous data suffer from large errors. A small error in the sensing synchronization may lead to a large discrepancy in the identified stiffness parameters. Moreover, it is seen that the updated stiffness parameters using modal parameters identified from the corrected spectral densities of the non-synchronous data are close to their actual values. The level of accuracy is comparable to that of the updated stiffness parameters using modal parameters identified from synchronous data.

Table 9 Modal frequencies and mode shapes identified by BSD

	Synchronous			Non- synchronous			Corrected non-synchronous		
Parameter	Optimal	SD	Error /MAC	Optimal	SD	Error /MAC	Optimal	SD	Error /MAC
f_1	1.7158	0.0017	-0.0058%	1.7713	0.0035	3.2286%	1.7157	0.0017	-0.0117%
f_2	5.0527	0.0032	0.0951%	5.1207	0.0607	1.4422%	5.0523	0.0032	0.0872%
f_3	8.0908	0.0055	0.0532%	8.3151	0.0086	2.8269%	8.0909	0.0055	0.0544%
f_4	10.6607	0.0091	0.0516%	10.8627	0.0181	1.9474%	10.6608	0.0091	0.0526%
ϕ_{11}	-0.1325	0.0005	1	-0.0301	0.0633	0.0184	-0.132	0.0018	1
ϕ_{12}	-0.2579	0.0005		-0.08	0.0632		-0.2582	0.0017	
ϕ_{13}	-0.3683	0.0005		0.0511	0.0633		-0.3686	0.0017	
ϕ_{14}	-0.4562	0.0004		0.8393	0.0344		-0.4554	0.0016	
ϕ_{15}	-0.5188	0.0004		0.0929	0.0631		-0.5185	0.0015	
ϕ_{16}	-0.5505	0.0004		-0.5263	0.0539		-0.5512	0.0015	
ϕ_{21}	-0.3678	0.0026	1	-0.2651	0.095	0.1099	-0.3555	0.0053	0.9998
ϕ_{22}	-0.5499	0.0023		0.9548	0.0293		-0.5546	0.0047	
ϕ_{23}	-0.4566	0.0025		-0.0678	0.0983		-0.4591	0.0051	
ϕ_{24}	-0.135	0.0027		-0.04	0.0984		-0.1303	0.0057	
ϕ_{25}	0.2575	0.0027		0.0183	0.0985		0.2537	0.0055	
ϕ_{26}	0.5189	0.0024		0.1076	0.0979		0.5234	0.0049	
ϕ_{31}	-0.5114	0.006	0.9997	-0.4083	0.0939	0.1454	-0.5314	0.0111	0.9994
ϕ_{32}	-0.372	0.0065		0.137	0.1018		-0.3531	0.0122	
ϕ_{33}	0.2495	0.0067		0.0141	0.1028		0.2564	0.0127	
ϕ_{34}	0.5544	0.0058		-0.8953	0.0458		0.5582	0.0109	
ϕ_{35}	0.1432	0.0069		-0.0187	0.1028		0.1323	0.013	
ϕ_{36}	-0.4583	0.0062		0.1114	0.1022		-0.445	0.0117	
ϕ_{41}	-0.5396	0.0117	0.9995	-0.943	0.0388	0.0733	-0.5489	0.0165	0.9993
ϕ_{42}	0.1447	0.0137		0.0773	0.1162		0.1365	0.0196	
ϕ_{43}	0.511	0.0119		-0.2536	0.1128		0.5027	0.0171	
ϕ_{44}	-0.2655	0.0134		0.1075	0.1159		-0.2711	0.0191	
ϕ_{45}	-0.4624	0.0123		0.1311	0.1156		-0.4704	0.0175	
ϕ_{46}	0.3774	0.0128		-0.108	0.1159		0.3642	0.0184	

Table 10 Updated stiffness parameters using modal data

		Synchronous			Non- synchronous			Corrected non-synchronous		
	Act-ual	Opti-mal	SD	Error	Opti-mal	SD	Error	Opti-mal	SD	Error
θ_1	-0.2	-0.1996	0.0005	-0.2%	0.2436	0.0032	-221.8%	-0.2022	0.0013	1.1%
θ_2	-0.2	-0.2011	0.0008	0.55%	-0.4351	0.0029	117.55%	-0.204	0.0015	2%
θ_3	-0.2	-0.1995	0.0007	-0.25%	1.3778	0.0512	-788.9%	-0.1971	0.0011	-1.45%
θ_4	-0.2	-0.2	0.0008	0%	-0.6022	0.0009	201.1%	-0.1995	0.0015	-0.25%
θ_5	-0.2	-0.1999	0.0008	-0.05%	967802	1093905	-4.8×10^8%	-0.2011	0.0012	0.55%
θ_6	-0.2	-0.2007	0.0007	0.35%	-0.3341	0.0005	67.05%	-0.1976	0.0011	-1.2%

7. Conclusions

The purpose of this paper is to address the problem of non-synchronous sensing on structural identification when using wireless sensor networks. The potential sources causing non-synchronous sensing are first discussed and the magnitudes of these errors are estimated based on time stamps collected from Imote2 sensors. Among these error sources the dominant ones are non-simultaneity in sensing start-up and differences in sampling frequency among sensor nodes. As shown in the simulation examples, these errors can distort the identified results of modal parameters and stiffness parameters. A small error in the sensing synchronization may lead to a large discrepancy in the identified mode shapes and stiffness parameters. A new methodology was proposed for eliminating such errors. This methodology estimates the power spectral density (PSD) of output responses using non-synchronous samples based on a modified FFT. Once the corrected spectral densities are obtained, the correlation functions can also be easily calculated by inverse Fourier transform. Then, these corrected PSDs or correlation functions can be fed into various output-only modal identification algorithms. Subsequently, stiffness parameters can be identified using modal-based structural model updating. Comparing with the resampling based signal reconstruction method, this method is simple, marginally more accurate and computationally efficient. It should be noted that this method is not applicable for some of the structural identification methods which are not based on power spectral densities or correlation functions and signal reconstruction may be necessary when using such methods for structural identification from non-synchronous data. The proposed correction method is validated using numerical simulations. The simulation results show that errors due to non-synchronous sensing are largely eliminated using the proposed method and the resulting identified parameters are of similarly accuracy as those estimated from synchronous data.

Acknowledgments

This research has been supported by the Hong Kong Research Grants Council under grants 613412 and 613713. These supports are gratefully acknowledged. The authors also would like to acknowledge Professor Billie F. Spencer Jr. and his group members from the University of Illinois at Urbana-Champaign for providing some of the codes used in these studies. Constructive comments from anonymous reviewers are also gratefully acknowledged.

References

Bendat, J.S. and Piersol, A.G. (1986), *Random Data: Analysis and Measurement Procedures (2nd Ed.)*, New York: Wiley.

Bendat, J.S. and Piersol, A.G. (1993), *Engineering Applications of Correlation and Spectral Analysis (2nd Ed.)*, New York: J. Wiley.

Brincker, R., Zhang, L. and Andersen, P. (2001), "Modal identification of output-only systems using frequency domain decomposition", *Smart Mater. Struct.*, **10**(3), 441-445.

Caicedo, J.M., Dyke, S.J. and Johnson, E.A. (2004), "Natural excitation technique and Eigensystem realization algorithm for phase I of the IASC-ASCE benchmark problem: Simulated data", *J. Eng. Mech. - ASCE*, **130**(1), 49-60.

Divi, V. and Wornell, G. (2008), "Bandlimited signal reconstruction from noisy periodic nonuniform samples in time-interleaved ADCS", *Proceedings of the In ICASSP, IEEE International Conference on Acoustics, Speech and Signal Processing* .

Felber, A.J. (1993), "Development of a hybrid bridge evaluation system", Ph.D. Dissertation, University of British Columbia (UBC), Vancouver, Canada.

Feng, Z. (2013), "Structural health monitoring using wireless sensor networks and Bayesian probabilistic methods", Ph.D. Dissertation, The Hong Kong University of Science and Technology.

Feng, Z. and Katafygiotis, L.S. (2013), "Efficient model updating with incomplete modal data for structural health monitoring", In Safety, Reliability, Risk and Life-Cycle Performance of Structures and Infrastructures - *Proceedings of the 11th International Conference on Structural Safety and Reliability*, ICOSSAR 2013.

James, G.H., Carne, T.G. and Lauffer, J.P. (1993), The Natural Excitation Technique (NExT) for modal parameter extraction from operating wind turbines (Vol. Rep. No. S). Sandia, NM: Sandia National Laboratories.

Juang, J.N. and Pappa, R.S. (1985), "An eigensystem realization algorithm for modal parameter identification and model reduction", *J. Guid. Control Dynam.*, **8**(5), 620-627.

Katafygiotis, L.S. and Yuen, K.V. (2001), "Bayesian spectral density approach for modal updating using ambient data", *Earthq. Eng. Struct. D.*, **30**(8), 1103-1123.

Kim, S., Pakzad, S., Culler, D., Demmel, J., Fenves, G., Glaser, S. and Turon, M. (2007), "Health monitoring of civil infrastructures using wireless sensor networks". In IPSN 2007: *Proceedings of the Sixth International Symposium on Information Processing in Sensor Networks*.

Krishnamurthy, V., Fowler, K. and Sazonov, E. (2008), "The effect of time synchronization of wireless sensors on the modal analysis of structures", *Smart Mater. Struct.*, **17**(5), 055018.

Lei, Y., Kiremidjian, A.S., Nair, K.K., Lynch, J.P. and Law, K.H. (2005), "Algorithms for time synchronization of wireless structural monitoring sensors", *Earthq. Eng. Struct. D.*, **34**(6), 555-573.

Li, J., Mechitov, K.A., Kim, R.E. and Spencer, B.F. Jr. (2015), "Efficient time synchronization for structural health monitoring using wireless smart sensor networks". *Struct. Control Health Monit.*, doi: 10.1002/stc.1782.

Lynch, J.P. (2007), "An overview of wireless structural health monitoring for civil structures". *Philosophical Transactions of the Royal Society A: Mathematical, Physical and Engineering Sciences*, **365**(1851), 345-372.

Lynch, J.P. and Loh, K.J. (2006), "A summary review of wireless sensors and sensor networks for structural health monitoring", *Shock Vib. Dig.*, **38**(2), 91-128.

Magalhães, F. and Cunha, Á. (2011), "Explaining operational modal analysis with data from an arch bridge", *Mech. Syst. Signal Pr.*, **25**(5), 1431-1450.

Maróti, M., Kusy, B., Simon, G. andLédeczi, Á. (2004), "The flooding time synchronization protocol". In SenSys'04 - *Proceedings of the Second International Conference on Embedded Networked Sensor Systems*.

Mukhopadhyay, S., Luş, H., Hong, A.L. and Betti, R. (2012), "Propagation of mode shape errors in structural identification", *J. Sound Vib.*, **331**(17), 3961-3975.

Nagayama, T. and Spencer, B.F. Jr. (2007), Structural Health Monitoring Using Smart Sensors (Vol. Report Ser). Urbana, IL: Newmark Structural Engineering Laboratory.

Nagayama, T., Sim, S.H., Miyamori, Y. and Spencer, B.F. Jr. (2007), "Issues in structural health monitoring employing smart sensors", *Smart Struct. Syst.*, **3**(3), 299-329.

Park, J.H., Kim, J.T. and Yi, J.H. (2011), "Output-only modal identification approach for time-unsynchronized signals from decentralized wireless sensor network for linear structural systems", *Smart Struct. Syst.*, 7(1), 59-82.

Peeters, B. and De Roeck, G. (1999), "Reference-based stochastic subspace identification for output-only modal analysis", *Mech. Syst. Signal Pr.*, **13**(6), 855-878.

Peeters, B. and De Roeck, G. (2001), "Stochastic system identification for operational modal analysis: A review", *J. Dynam. Syst. Measurement Control*, **123**(4), 659.

Peeters, B., Van der Auweraer, H., Guillaume, P. and Leuridan, J. (2004), "The PolyMAX frequency-domain method: A new standard for modal parameter estimation?", *J. Shock Vib.*, **11**(3-4), 395-409.

Shen, W., Lei, Y., Hu, L. and Wang, Y. (2012), "Feasibility of output-only modal identification using wireless sensor network: A quantitative field experimental study", *Int. J. Distrib. Sens. N.*, 2012, 1-17.

Sundararaman, B., Buy, U. and Kshemkalyani, A.D. (2005), "Clock synchronization for wireless sensor networks: A survey", *Ad Hoc Networks*, **3**(3), 281-323.

Wang, Y., Swartz, R.A., Lynch, J.P., Law, K.H., Lu, K.C. and Loh, C.H. (2007), "Decentralized civil structural control using real-time wireless sensing and embedded computing". *Smart Struct. Syst.*, **3**(3), 321-340.

Welch, P.D. (1967). "The use of fast fourier transform for the estimation of power spectra: A method based on time averaging over short, modified periodograms", *IEEE T. Audios and Electroacoustics*, AU-15, 70-76.

Yan, G. and Dyke, S.J. (2010), "Structural damage detection robust against time synchronization errors", *Smart Mater. Struct.*, **19**(6), 065001.

Appendices

Appendix I. Derivation of Eq. (8)

In time domain, the non-synchronous data is expressed as in Eq. (3): $x(t_k{}') = x(\alpha t_k + \delta)$. The finite Fourier transform of the non-synchronous data

$$X'_T(f) = \int_0^T x(\alpha t + \delta) e^{-j2\pi ft} dt \tag{25}$$

Let $\lambda = \alpha t + \delta$, then $t = \dfrac{\lambda - \delta}{\alpha}$

$$\begin{aligned} X'_T(f) &= \int_0^T x(\alpha t + \delta) e^{-j2\pi ft} dt \\ &= \int_0^T x(\lambda) e^{-j2\pi f(\frac{\lambda-\delta}{\alpha})} d(\frac{\lambda - \delta}{\alpha}) \\ &= \frac{1}{\alpha} e^{j2\pi f\frac{\delta}{\alpha}} \int_0^T x(\lambda) e^{-j2\pi(\frac{f}{\alpha})\lambda} d\lambda \\ &= \frac{1}{\alpha} e^{j2\pi f\frac{\delta}{\alpha}} X_T(\frac{f}{\alpha}) \end{aligned} \tag{26}$$

Appendix II. Derivation of Eq. (19)

The discrete Fourier transform for shifted $\mathbf{x}'_\beta$ is given by

$$\begin{aligned} X'_\beta(f_k) &= \sum_{n=0}^{n=N-1} x_\beta(n\Delta t + \delta) e^{-j2\pi f_k n\Delta t} \\ &= \sum_{n=0}^{n=N-1} x_\beta(n\Delta t + \delta) e^{-j2\pi f_k (n\Delta t + \delta)} \cdot e^{j2\pi f_k \delta} \\ &= e^{j2\pi f_k \delta} \cdot \sum_{n=0}^{n=N-1} x_\beta(n\Delta t + \delta) e^{-j2\pi f_k (n\Delta t + \delta)} \\ &= e^{j2\pi f_k \delta} \cdot X_\beta(f_k) \end{aligned} \tag{27}$$

Appendix III. Derivation of Eq. (21)

$$
\begin{aligned}
S_{x_\alpha x_\beta}(f_k) &= \lim_{T\to\infty}\frac{1}{T}E\left[X^*_\alpha(f_k,T)\cdot X_\beta(f_k,T)\right]\\
&= \lim_{T\to\infty}\frac{1}{T}E\left[\left(\int_0^T x_\alpha(t)e^{-j2\pi f_k t}dt\right)^*\cdot\left(\int_0^T x_\beta(t)e^{-j2\pi f_k t}dt\right)\right]\\
&= \lim_{T\to\infty}\frac{1}{T}E\left[\int_0^T x_\alpha(t)e^{j2\pi f_k t}dt\cdot\int_0^T x_\beta(t)e^{-j2\pi f_k t}dt\right]\\
&= \lim_{N\to\infty}\frac{1}{N\Delta t}E\left[\Delta t\sum_{n=0}^{N-1}x_\alpha(n\Delta t)e^{j2\pi f_k n\Delta t}\cdot\Delta t\sum_{n=0}^{N-1}x_\beta(n\Delta t)e^{-j2\pi f_k n\Delta t}\right]\\
&= \lim_{N\to\infty}\frac{\Delta t}{N}E\left[\sum_{n=0}^{N-1}x_\alpha(n\Delta t)e^{j2\pi f_k n\Delta t}\cdot\sum_{n=0}^{N-1}x_\beta(n\Delta t)e^{-j2\pi f_k n\Delta t}\right]\\
&= \lim_{N\to\infty}\frac{\Delta t}{N}E\left[X^*_\alpha(f_k)X_\beta(f_k)\right]
\end{aligned}
\tag{28}
$$

Appendix IV Derivation of Eq. (23)

$$
\begin{aligned}
S_{x_\alpha x_\beta}(f_k) &= \lim_{T\to\infty}\frac{1}{T}E\left[X^*{}_\alpha(f_k,T)\cdot X_\beta(f_k,T)\right]\\
&= \lim_{T\to\infty}\frac{1}{T}E\left[\left(\int_0^T x_\alpha(t)e^{-j2\pi f_k t}dt\right)^*\cdot\int_0^T x_\beta(t)e^{-j2\pi f_k t}dt\right]\\
&= \lim_{T\to\infty}\frac{1}{T}E\left[\int_0^T x_\alpha(t)e^{j2\pi f_k t}dt\cdot\int_0^T x_\beta(t)e^{-j2\pi f_k t}dt\right]\\
&= \lim_{N_\alpha\to\infty}\frac{1}{N_\alpha\Delta t_\alpha}E\left[\Delta t_\alpha\sum_{n_1=0}^{N_\alpha-1}x_\alpha(n_1\Delta t_\alpha)e^{j2\pi f_k n_1\Delta t_\alpha}\cdot\Delta t_\beta\sum_{n_2=0}^{N_\beta-1}x_\beta(n_2\Delta t_\beta)e^{-j2\pi f_k n_2\Delta t_\beta}\right]\\
&= \lim_{N_\alpha\to\infty}\frac{\Delta t_\beta}{N_\alpha}E\left[\sum_{n_1=0}^{N_\alpha-1}x_\alpha(n_1\Delta t_\alpha)e^{j2\pi f_k n_1\Delta t_\alpha}\cdot\sum_{n_2=0}^{N_\beta-1}x_\beta(n_2\Delta t_\beta)e^{-j2\pi f_k n_2\Delta t_\beta}\right]\\
&= \lim_{N_\alpha\to\infty}\frac{\Delta t_\beta}{N_\alpha}E\left[X^*_\alpha(f_k)X_\beta(f_k)\right]\\
&= \lim_{N_\beta\to\infty}\frac{\Delta t_\alpha}{N_\beta}E\left[X^*_\alpha(f_k)X_\beta(f_k)\right]
\end{aligned}
\tag{29}
$$